International Journal of Adhesion and Adhesives 95 (2019) 102395

Contents lists available at ScienceDirect

International Journal of Adhesion and Adhesives

journal homepage: www.elsevier.com/locate/ijadhadh

Experimental investigation and numerical modelling of the mechanical response of a semi-structural polyurethane adhesive

John Fredrick Berntsen[a,b,*], David Morin[a,b], Arild Holm Clausen[a,b], Magnus Langseth[a,b]

[a] Structural Impact Laboratory (SIMLab), Department of Structural Engineering, Norwegian University of Science and Technology (NTNU), NO-7491, Trondheim, Norway
[b] Centre for Advanced Structural Analysis (CASA), NTNU, NO-7491, Trondheim, Norway

ARTICLE INFO

Keywords:
A. Polyurethane
C. Finite element stress analysis
D. Mechanical properties of adhesives

ABSTRACT

The use of adhesives in load-carrying structures and components has increased recently, especially in the automotive industry. There has been many studies on structural adhesives, but when it comes to semi-structural adhesives, there is a lack of literature. In this article, a semi-structural two component polyurethane adhesive has been studied experimentally and modelled numerically. It was performed uniaxial tension tests at rates ranging from $10^{-3}s^{-1}$ to $10^{-1}s^{-1}$. The tests were monitored by two perpendicular digital cameras and a thermal camera. Similarly, uniaxial compression tests were performed at rates ranging from $10^{-3}s^{-1}$ to $350s^{-1}$, where a split Hopkinson pressure bar (SHPB) was used for the highest rates. The low-rate tests were recorded with high-resolution digital cameras, while a high-speed camera and a thermal camera were used for the SHPB tests. In addition, it was performed notched tensile tests at a low rate to study failure. These tests also served as a validation case for the numerical simulations. A high-resolution camera was used, such that the local strains in the notch could be captured using digital image correlation. The experiments indicated that the adhesive behaved similar as rubbers. Therefore, the Bergström-Boyce constitutive model was applied in the numerical simulations. The overall prediction of the test results was seen to be satisfactory, but the initial stiffness was too high compared to the response measured from the experiments. An investigation of the numerical results indicated that this mismatch was likely linked to the formulation of the inelastic shear rate.

1. Introduction

In recent years, there has been an increased use of adhesive bonding in the industry, especially in the automotive industry. A driving factor for this development has been the pursuit of lightweight design. The evolution of car bodies calls for an optimal combination of materials of different nature, i.e., steel, aluminium, polymers and composites. These multi-material car bodies utilize the benefits of each class of materials by applying them in strategic parts of the structure. While traditional steel car frames extensively have utilized spot-welding as the main joining technique, these new generations of car bodies require new joining technologies as welding might not be possible. An efficient manner of joining these fundamentally different materials is through adhesive bonding. There are two types of adhesives applied for this purpose; structural and semi-structural adhesives. Structural adhesives are characterized by their high stiffness and strength. These adhesives, often referred to as crash-stable adhesives, are used to increase the overall stiffness of a car body but also to improve their crash performance. Semi-structural adhesives have lower strength and significantly lower stiffness. In addition to being used as sealants, these adhesives can also be applied to join a wider range of materials than the structural adhesives as they do not require heat input to solidify. However, they are often based on two reactive components. Within the framework of the automotive industry, joints incorporating adhesives are exposed to extreme loadings, with both large deformations and a high rate of deformation. According to Martinsen et al. [1] there is currently a lack of understanding in both the behaviour of these type of joints as well as how to model them with confidence.

Following the trend in the industry, there has been a significant development within the field of adhesive testing in recent years. A comprehensive overview is presented in the work by da Silva et al. [2], which describes a range of experiments designed to characterize adhesives. There are two main approaches to characterize an adhesive. The most common approach is to characterize the adhesive as a part of an assembly, determining energy release rate for the relevant global deformation modes as done by Hasegawa et al. [3]. This is a high-level approach, where the gradients through the adhesive layer are not considered, meaning that the results are dependent on the assembly.

* Corresponding author. Department of Structural Engineering, NTNU, Richard Birkelands vei 1A, 7491, Trondheim, Norway.
E-mail address: john.f.berntsen@ntnu.no (J.F. Berntsen).

https://doi.org/10.1016/j.ijadhadh.2019.102395

Available online 04 June 2019

The second approach considers the adhesive itself independent of the adherents, with a goal of determining local behaviour of the adhesive in detail. This kind of experiments are typically performed on bulk adhesive test specimens with simple geometries, such that the stress and strain fields in the region of interest could be determined through simple manipulations. This information is then used to characterize a constitutive relation for the adhesive at hand. Dufour et al. [4] shows how uniaxial tension and compression tests were used to characterize a structural adhesive in this manner. This is a low-level approach, which enables a more detailed analysis of the mechanical behaviour in the adhesive layer. Therefore, it was chosen as the approach applied in this work. Furthermore, validation of a constitutive model should consider the global response of an assembly, as seen in the article by Campilho et al. [5]. Any specimen with a non-trivial deformation field could act as a validation case.

A key phenomenon during crash loading is the rate sensitivity of the material. Split-Hopkinson bar techniques are commonly applied to achieve strain rates relevant for crash applications. Jia et al. [6] showed that the behaviour of a semi-structural adhesive could change drastically for increased strain rates. It should be noted that the measurements performed by Jia et al. [6] assumed a uniform strain field in the gage section of the specimens. Morin et al. [7] applied digital image correlation (DIC) to evaluate the in-plane strain field of similar specimens, and they found that the assumption of homogeneous deformation might not be valid for this type of materials. They have also shown that adhesives can exhibit pressure sensitivity by comparing the response in tension and compression tests. Furthermore, DIC could also be used to identify incompressibility and measure large strains, which are phenomena that are commonly found in flexible adhesives [8]. Numerical simulations in combination with experiments could reveal additional information, as Morin et al. [9] displayed by evaluating the dependency of stress tri-axiality ratio with respect to failure. It is evident that an extensive experimental campaign with state of the art measurement techniques is needed to identify which phenomena are governing the mechanical behaviour of a given adhesive.

There are two common approaches for numerical modelling of adhesives. Macroscopic models such as cohesive zone models (CZM), defined by a traction separation law, are used for large-scale analysis due to the low computational cost as well as their simplicity. A state-of-the-art CZM model was presented by Morin et al. [10]. This model captures a range of phenomena typically observed in structural adhesives including viscoplasticity and pressure sensitive yield surface as well as accounting for crack propagation velocity. The other approach is to use mesoscopic models. In these models, the adhesive layer is discretized by a fine solid element mesh where a constitutive model defining the relationship between the stresses and strains of the material is used. An example of mesoscale modelling is seen in the work by Dufour et al. [4], while a comparison between the two approaches is provided by Leuschner et al. [11]. A mesoscopic model allows for fine discretization that could be used to study the local behaviour in an adhesive joint where a macroscopic model does not possess the appropriate accuracy. Applying a suitable mesoscopic model, it could reveal information that is not available from current experimental techniques. The influence of different adherents could be further studied using this methodology. Information obtained through this process could then be used to either improve existing macroscopic models or develop new ones for the use in large-scale analysis.

The numerical models described so far are typically developed to describe structural epoxy-based adhesives. There is considerably less literature suited for the softer semi-structural polyurethane adhesives. Duncan and Dean [8] suggested using hyperelastic models to account for the large elastic deformations observed for this type of adhesives. Lubowiecka et al. [12] reported promising results for quasi-static tests using a Neo-Hookean model. Considering the intended applications in the automotive industry, it is important to account for the dynamic properties as well. Golaz et al. [13] used a hyperelastic Ogden fit in combination with a two-term Prony series to model a thermoplastic polyurethane, showing a good fit for that specific case.

A significant limitation with an Ogden series fit is that it requires calibration of many parameters. In addition, this model is entirely phenomenological, such that there is uncertainty in the behaviour in loading modes not used for the calibration. According to data presented by Bergström [14], the simpler Bergström-Boyce (BB) model [15] shows promising results for rubbers. In addition to being simpler, the expected behaviour in other loading modes is likely to be more accurate as the model is based on micromechanical considerations. Bergström and Boyce suggested that the response of a polymer is comprised of two contributions, one rate independent and one rate dependent. It was assumed that the rate independent response was due to network stretching, modelled by the Arruda-Boyce eight-chain model [16]. Free chains subjected to affine stretching and relaxation due to reptation were assumed for the rate dependent response, leading to a primarily additive rate sensitivity. The BB model is easily calibrated if it is found suitable for a given adhesive.

In this work, a range of experimental methods has been applied to identify the key phenomena governing the mechanical behaviour of the semi-structural Betaforce 2816L adhesive. The results of the experiments have been used to determine, calibrate and validate two suitable material models at a mesoscopic scale. These models are better suited than those currently employed in the literature for this type of adhesives. Further, they should facilitate future studies on the influence of multi-material joining for adhesively bonded joints. A description of the performed experiments will be provided in the next section. Thereafter, the post-processed results from the experiments will be presented in Section 3. Those results will further be used in Section 4 to calibrate and validate the chosen numerical models. Finally, the results of the experiments in combination with the simulations will be discussed before the article is rounded off with some concluding remarks.

2. Experimental

2.1. Materials and test specimens

The semi-structural two-component adhesive Betaforce 2816L with density 1310 kg/m^3 is studied in this work. Produced by DOW, this adhesive is characterized by the good adhesion to a range of materials, and the curing takes place in room temperature. It is currently in use in the automotive industry.

In the preparation phase of the experimental campaign, the electrical adhesive gun BETAGUN with a dynamic mixing bridge was used to mix and distribute the two components of the adhesive. Depending on their geometry, the adhesive specimens were created using two different processes. Tension test and notched tension test specimens were cut from 2mm thick plates, which were created using hydrostatic pressure based on the principles outlined by da Silva et al. [2]. This thickness as well as the adhesive gun corresponds to what is used in the technical datasheet for this adhesive. Therefore, it is believed that the specimens machined from these plates should be comparable to real applications of this adhesive. Compression test specimens were cut from a cylinder with a diameter of 51mm. The cylinders were created by pouring the adhesive directly into the cylindrical mould. While pouring the adhesive, the nozzle of the gun stayed in contact with the rising surface of the adhesive to avoid formation of voids. Due to heat generation during curing, the cylindrical mould had to be cooled in a water bath to avoid overheating. Finally, all specimens were machined using water-jet cutting, as the material was too soft to operate on with typical machining tools. It should be noted that the cut surfaces of the specimens were not perfectly smooth, and that the edges on the cylindrical specimens were slightly slanted. Final geometry of bulk adhesive specimens are presented in Fig. 1. There was not performed any sensitivity study with respect to production parameters, as it was considered out of scope for this article.

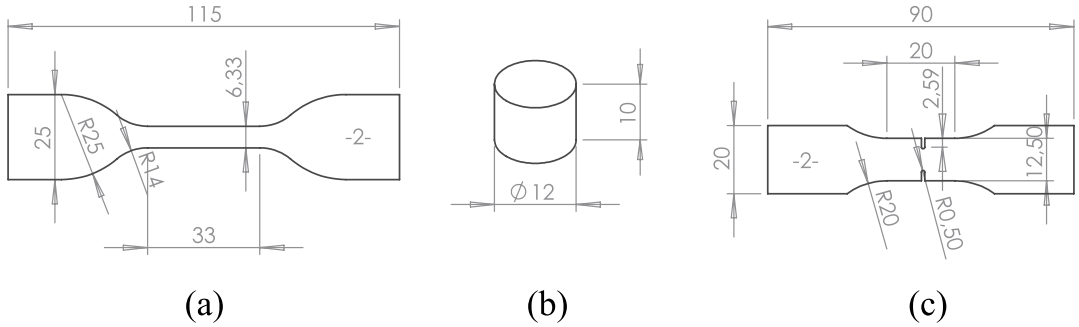

Fig. 1. Geometry of bulk adhesive specimens. Measures in mm. (a) Uniaxial tensile specimen (ISO 37). (b) Compression specimen. (c) Notched specimen.

In order to identify porosities or inclusions within the test specimens, computed tomography (CT) scans of several specimens were performed. A voxel size of 0.0058mm was achieved with the selected settings. The gauge section of three tension specimens was scanned, uncovering one single void having length of 0.6mm along its major axis, accounting for roughly 1% of the cross sectional area and 0.001% of the studied volume. These results suggested that the porosity should have a negligible effect on the measured stresses and strains. It should also be noted that there were observed multiple smaller volumes with lower density, having a maximum dimension of approximately 0.1mm. This could indicate that there are small pockets of unmixed adhesive.

Table 1
Test matrix for bulk adhesive testing.

Specimen type	Test machine	Nominal rate [s^{-1}]	Number of repetitions	Camera logging frequency [s^{-1}]
Tensile	Instron 2kN hydraulic	10^{-3}	6	1
		10^{-2}	10	10
		10^{-1}	8	15
Compression	Instron 2kN hydraulic	10^{-3}	5	1
		$5{\cdot}10^{-2}$	5	15
	SHPB	~ 300	5	75000
Notched	Instron 2kN hydraulic	$2{\cdot}10^{-2}$	6	1

2.2. Experimental configurations

The tension tests were performed on an Instron 5944 hydraulic machine equipped with a 2kN load cell, using the specimen shown in Fig. 1a. To facilitate for DIC, the specimens were coated with a speckled pattern. Two perpendicular cameras of type Prosilica GC2450 were used to capture both the front and side surface of the dog-bone specimens as illustrated in the section view of Fig. 2a. In addition, the rear surface of the specimen was coated with matte black spray-paint to ensure high emissivity corresponding to the calibration of an infrared camera of type FLIR SC 7500. The tension tests were run at three different nominal strain rates ranging from $10^{-3}s^{-1}$ to $10^{-1}s^{-1}$, corresponding to cross-head velocities of respectively 1.98mm/s, 19.8mm/s and 198mm/s. It should be noted that the specimens were made in three different batches, with the first batch covering the entire range of strain rates. The second batch was only tested for the rates $10^{-3}s^{-1}$ and $10^{-2}s^{-1}$, and the last batch for the rates $10^{-2}s^{-1}$ and $10^{-1}s^{-1}$. For full test matrix, see Table 1.

Compression tests were performed on the cylindrical specimens shown in Fig. 1b. The first set of compression tests were carried out with the same hydraulic machine as in the tension tests. The configuration is shown in Fig. 2b, and the applied nominal strain rates were $10^{-3}s^{-1}$ and $5{\cdot}10^{-2}s^{-1}$, or respectively 0.6mm/s and 30mm/s. These specimens were also coated with a speckled pattern to facilitate DIC using two perpendicular cameras. A second set of compression tests were run in a split-Hopkinson pressure bar (SHPB) setup to achieve strain rates up to $350s^{-1}$. One side of the specimens was coated with the speckled pattern for DIC, and the other with matte black spray-paint for the infrared camera. A schematic figure of the SHPB setup with dimensions is shown in Fig. 3. The bars used in this experiment were 16mm diameter steel bars, and the high-speed camera was a Phantom v161 recording at 75000Hz.

The notched tension tests were performed with the same machine as the tension tests, using the specimen geometry and configuration shown in Figs. 1c and 2c, respectively. Preliminary numerical simulations were used to determine the radius of 0.5mm in the notch in order to achieve a stress triaxiality ratio of 0.4 at failure. A constant cross-head velocity

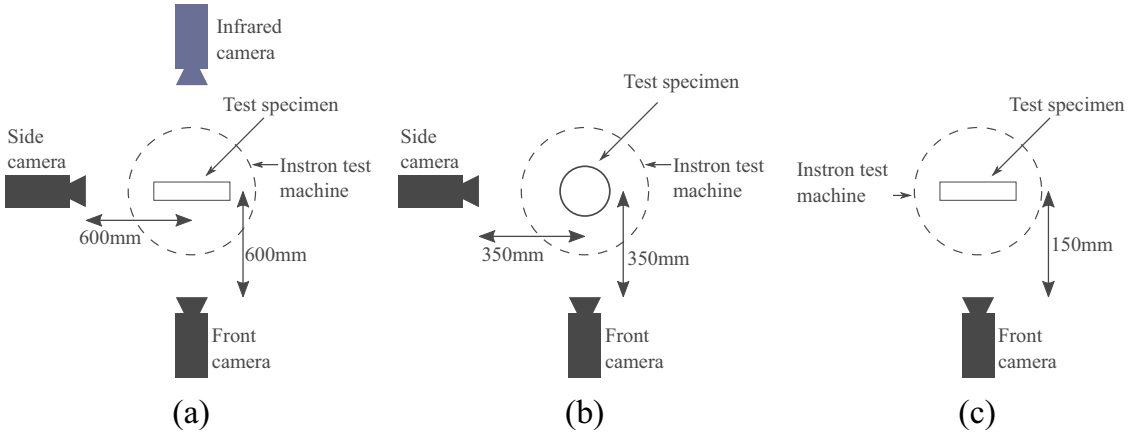

Fig. 2. Schematic cross section view as seen from above of quasi-static test setups applying the Instron 2kN hydraulic test machine. (a) Uniaxial tensile test setup. (b) Compression test setup. (c) Notched test setup.

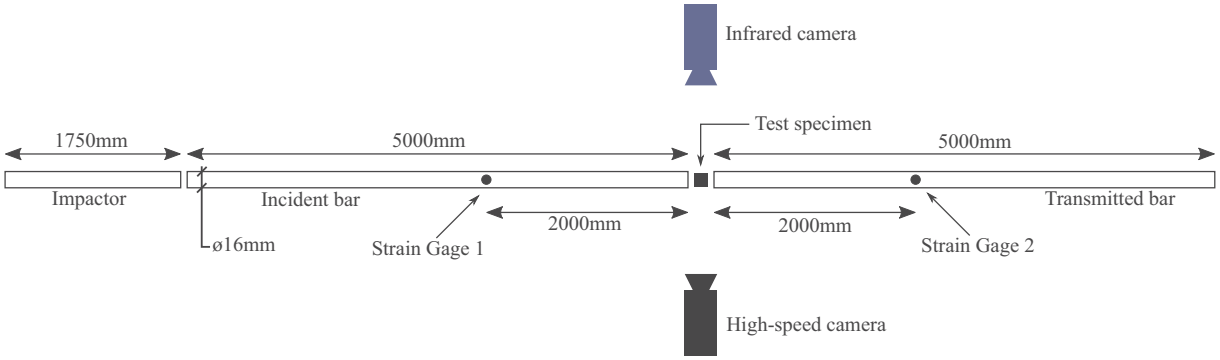

Fig. 3. Schematic figure of SHPB setup.

of 1.2mm/s was applied in these tests. Field deformations in the notch were obtained using DIC on images captured by a high-resolution camera monitoring the front surface of the specimen. This enabled retrieval of the local failure strain inside the notched region of the specimen, see Section 3.4.

3. Experimental results

3.1. Uniaxial tensile test results

Results from representative uniaxial tension tests are presented in Fig. 4. These results are in accordance with what is reported in the technical datasheet of the adhesive, although those data were obtained with different methods. The digital pictures taken during the tests were analysed with DIC in order to obtain the strain field data. Initial studies with a large amount of elements suggested that the strain field was uniform in the gauge section. Thus, the decision of which element and size to use was based on minimizing the DIC error. Therefore, the DIC analysis was performed using linear elements with a size of 50px × 50px, corresponding to 1.8 mm × 1.8 mm, for both the front and the side camera. An example of a strain field obtained with these parameters is presented in Fig. 4a.

Since the strain field was rather homogeneous over the entire gauge length at all stages of deformation, virtual extensometers (VE) were applied to the deformation fields obtained from DIC to determine the strains. The initial length of these VE spanned the length, width and thickness directions of the gauge section to further reduce the DIC error. It is evident from the transverse strain data shown in Fig. 4b that the material exhibits a close-to-isochoric behaviour. This represents a significant difference from the observations previously made by Dufour et al. [4] and Morin et al. [7] on crash-stable epoxy adhesives. Large volumetric deformations in the plastic domain were reported in both these studies. The Cauchy stress presented in Fig. 4c is computed based on the assumption of incompressibility.

A key observation from the results presented in Fig. 4c is the presence of rate sensitivity. Going from a nominal rate of $10^{-3}s^{-1}$ to $10^{-1}s^{-1}$ yields a 15% increase in stress level for the representative curves. Additionally, it is clear that this rate sensitivity behaves in a multiplicative manner, with a gradually increasing viscous overstress as the stress level increases. The residual strains in the specimens after failure were estimated by measuring the length before and after conducting the tests. An upper limit of the residual strains was found to be around 1%. Thus, the plastic strains could be considered negligible for this material.

There was observed significant scatter in the stress level of the material, with up to 10% deviation from the average response at a given strain as seen in Fig. 4d. This scatter is mainly observed between the three different batches of specimens, indicating some variations in the production process. A potential source may be the density of the inhomogeneity described in Section 2.1. Therefore, the representative curves presented in Fig. 4c are all from the same batch representing the average response. There was also observed scatter in the longitudinal logarithmic strain at failure, varying from 0.55 to 0.75. Scatter in failure strain was seen to be independent on the batch of specimens, as it is likely to be dominated by the size and location of a critical defect.

3.2. Uniaxial compression test results

Representative data from the compression tests are presented in Fig. 5a. Similar to the tension tests, field data was obtained using DIC. Initial studies revealed that the compression specimens exhibited a non-uniform deformation field. It was also discovered that parts of the specimens were not properly in focus leading to minor correlation issues for the DIC. Therefore, linear DIC elements with size of 100px × 100px corresponding to 1.1mm × 1.1mm were chosen as a compromise for the low rate tests. For the SHPB tests, the high-speed camera had a much lower image resolution, resulting in DIC element size of 30px × 30px equal to 1.5mm × 1.5mm.

The compression tests were performed only on a single batch, thus the variation as seen in Fig. 5b is significantly less than what was observed for the tension tests. SHPB experiments, which were run at much higher strain rates than the tests on the hydraulic machine, confirmed that rate sensitivity is an important component of the behaviour of the material. This aspect of the investigated adhesive is of high importance in industrial applications, where the adhesive layers could be subjected to high-rate loading.

In Fig. 5c, the gradient in the vertical direction was likely caused by the imperfections mentioned in Section 2.1. Especially the slightly slanted edges would lead to the observed non-uniformity. Using numerical simulations with slanted edges, it was verified that an average strain measure and an average stress measure represent the uniaxial behaviour of the material. Thus, the strains presented in Fig. 5a are based on a virtual extensometer retrieving the average strains from the deformation field obtained through DIC. The average strains also have the advantage of eliminating the extreme values observed in Fig. 5c, which are believed to be caused by DIC error.

The specimens experienced barrelling during the tests. This was accounted for by measuring the curvature of the boundary of the specimens using edge tracing, such that data could be omitted from the stage where the change in curvature started to grow. Barrelling occurred at a strain around 0.2. The compression specimens display the same phenomena as the tension specimens, showing incompressibility, rate sensitivity and negligible residual strains. It can also be seen from Fig. 6 that the response is similar in tension and compression when scatter is accounted for. This indicates that the adhesive is not very sensitive to the thickness of the adhesive layer, as the tension and compression specimens were cut from two different bulks of adhesive as described in Section 2.1.

A common issue with SHPB tests on polymers is that the transmitted signal has a very low magnitude compared to the noise. As seen in Fig. 5d, the noise oscillates in a random manner around a smooth

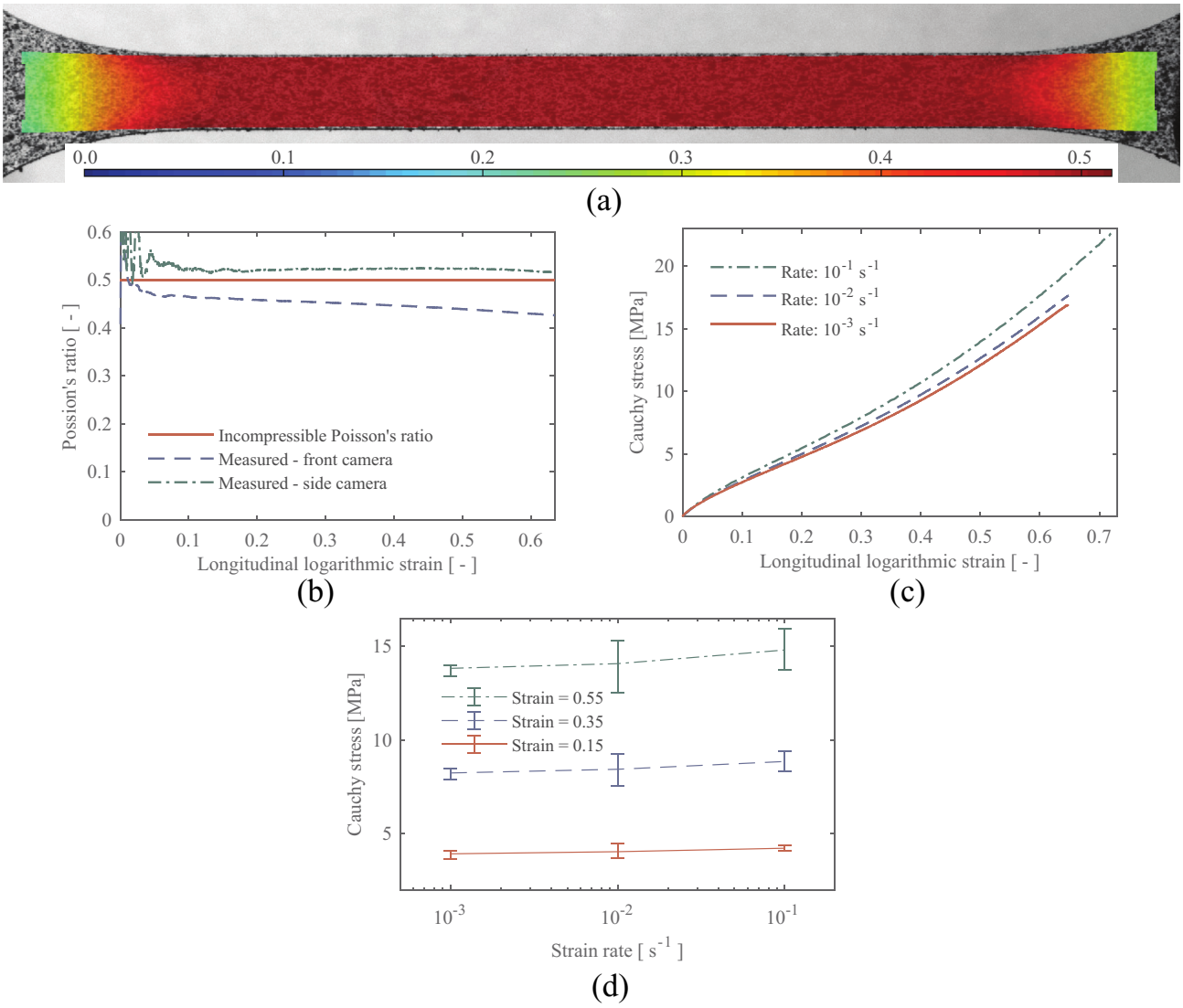

Fig. 4. Uniaxial tension test results. (a) Logarithmic strain field obtained from a DIC analysis of a tension test specimen. (b) Measured Poisson's ratios plotted against logarithmic strain for a representative tension test at a nominal strain rate of $10^{-2}s^{-1}$. (c) Representative Cauchy stress vs. logarithmic strain curves from uniaxial tension tests at 3 different nominal strain rates. (d) Scatter in tension stress at three strain levels for three different strain rates.

average signal. A reasonable estimate of the response was obtained using local regression with weighted linear least square fit smoothing. This estimate is considered suitable to determine the magnitude of the rate sensitivity.

3.3. Thermal results

Representative data collected through the infrared camera from tests at the highest rate in both tension and compression are presented in Fig. 7. Apparently, there was a minor initial temperature gradient in the compression specimens. Therefore, it was necessary to track individual points on the surface of the specimens to determine the change of temperature. With that accounted for, the observed temperature increase for the tension test and the SHPB compression test were 2.9K and 2.0K, respectively. Both the rate of deformation and the final state of strain were significantly different for the two displayed cases. The tension test was run at a nominal strain rate of $10^{-1}s^{-1}$ until a strain of 0.7, while the SHPB compression test was run at a nominal rate of $350s^{-1}$ until a strain of -0.5. It is believed that the compression test experienced near adiabatic conditions due to the high rate of deformation. The tension test was run at a much lower rate, but results from Johnsen et al. [17] indicate that a significant temperature increase could be measured even at a nominal rate of $10^{-1}s^{-1}$ for a polymer.

It should be noted that the temperature measurements on the SHPB tests are subjected to significantly more uncertainty than the tension tests. This is because the frequency of the thermal camera for the SHPB tests was only at 1125Hz, while the sampling rate of the temperature data was similar to the DIC cameras for the tension tests. However, this error was bounded by the difference between the frames at roughly 0.5K. Overall, the thermal data suggest that the potential change in temperature due to self-heating is limited to a few Kelvin, even at the highest rates. The reason for the negligible self-heating is believed to be the low stress level and lack of plastic deformation.

3.4. Notched tension test results

Fig. 8a shows pictures of one of the notched tension samples at four stages during the test. These tests were run to investigate fracture in the adhesive when subjected to an increased stress triaxiality ratio. Additionally, they served as a validation case for the numerical simulations due to their non-uniform stress field. Field data from the tests were retrieved through two separate DIC analyses. To investigate fracture, a DIC analysis with quadratic elements of the size 50px × 50px corresponding to 0.36mm × 0.36mm was used. In this

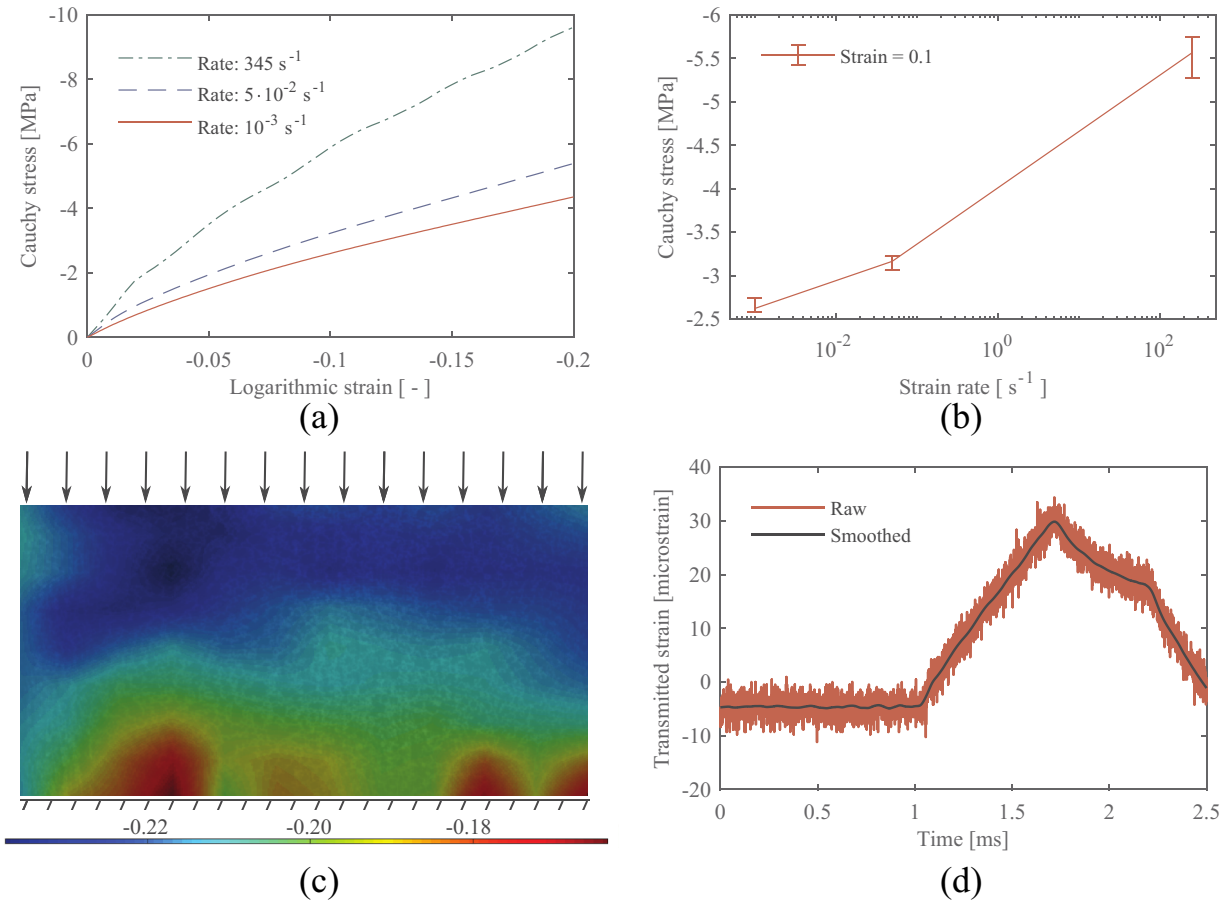

Fig. 5. Uniaxial compression test results. (a) Representative Cauchy stress vs. logarithmic strain curves from uniaxial compression tests at 3 different nominal strain rates. (b) Scatter in compression stress at a strain level of 0.1 for three different strain rates. (c) Example of DIC on compression specimen tested at a nominal strain rate of $10^{-3}s^{-1}$. (d) Comparison between raw data and smoothed SHPB data.

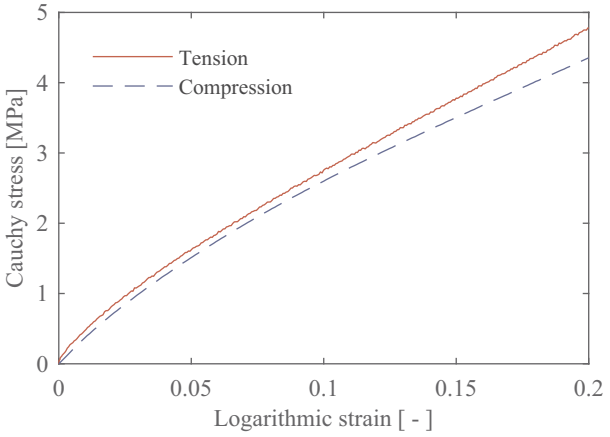

Fig. 6. Comparison between compression and tension response at a nominal strain rate of $10^{-3}s^{-1}$.

case, quadratic elements were chosen due to the large strain gradients in this critical region of the specimens. Based on this deformation field, a local strain measure was defined using a virtual extensometer (VE) with a length of 0.1mm. This VE was located at the front surface of the specimens in the most critical region, which was typically at the centre vertex of the notch, see the exaggerated part of Fig. 8b. Further, a nominal deformation measure was based on a separate DIC analysis using linear elements of the same size at the centre of the entire notched region. The nominal strain was then defined by applying a VE to this field, with initial length of 1.0mm corresponding to the notch diameter as illustrated in Fig. 8b. Finally, the nominal stress was found by dividing the global force with the minimum initial cross-section area.

Fig. 8c shows the nominal stress vs. nominal strain of all replicate tests, where failure initiation is marked with a '×'. It is seen that there is a large scatter in stress level, nominal failure strain and time from initiation of failure to complete loss of force-carrying capability. The local strain measure was used to determine failure. It can be seen from the representative test in Fig. 8d that the local strain experienced a significant increase prior to complete loss of force-carrying capability. This growth in local strain rate indicates the initiation of crack propagation, which has been used to define failure. Further, it should be noted that this failure definition captures the initiation of crack propagation before it was visible on the surface of the specimen as seen in Fig. 8a.

The local strain at initiation of crack propagation was measured to be in the range of 0.80 to 0.86. This is significantly less scatter than for the nominal strain, which varies from 0.2 to 0.3 at failure initiation. It was also seen from the images of the specimens that the location of the crack initiation varies. This is counter-intuitive considering the elevated stress triaxiality ratio and stress level in the centre of the notch. It is likely that crack initiation and failure for this material are dominated by initial flaws at the surface of the specimens. Thus, the source of the variation would be due to imperfections in the production process. Specifically for these specimens with a sharp notch, the water-jet cutting was not precise enough to avoid significant flaws. While there were no voids observed on the fractured surfaces, there might also have been internal flaws due to imperfect mixing of the adhesive components as mentioned in Section 2.1.

Scanning electron microscopy (SEM) was used to inspect the fracture surface of one of the notched specimens. A typical section of the

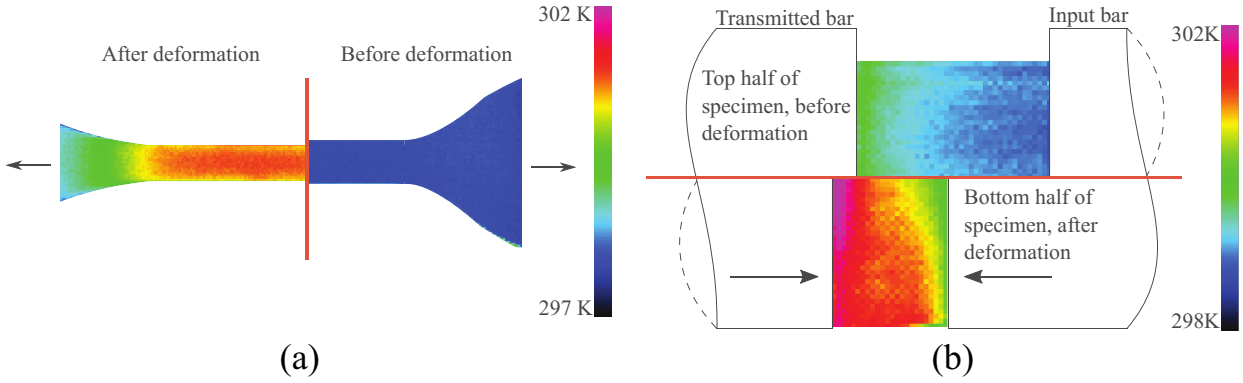

Fig. 7. Temperature measurements for different tests at different rates. (a) Temperature measurements of a tension test at a nominal strain rate of $10^{-1}s^{-1}$. (b) Temperature measurements of a SHPB compression test at a nominal strain rate of $350s^{-1}$.

fractured surface is shown in Fig. 9a. There are no features like dimples, ridges or fibrils, which would indicate ductile failure. Thus, the common failure models suggested by Duncan and Dean [8] for structural adhesives are not applicable in this case. Furthermore, the failure was brittle in the sense that there were no plastic deformations. However, large elastic deformations allow it to behave in an overall ductile manner, despite the failure mechanism being brittle. Fig. 9b shows the area in which it is believed that failure initiated. The irregular topology in the highlighted region enforces the assumption that failure was initiated by an initial imperfection.

4. Numerical modelling

4.1. Constitutive modelling

It has been demonstrated in Section 3 that the key phenomena for this semi-structural adhesive are incompressibility, large elastic deformations, rate sensitivity, and insignificant permanent deformation and self-heating. These phenomena were observed in all replicates of the experiments, indicating that the modelling approach should be independent on any scatter described in Section 3. In summary, the behaviour is similar in nature to typical rubber materials. Thus, candidate models for this material include: Neo-Hooke (NH), Arruda-Boyce eight-chain (AB), Mooney-Rivlin (MR), Ogden (OG) with linear viscoelasticity, and Bergström-Boyce (BB) with a non-linear viscous response. Initial calibration efforts indicated that both a NH model and an AB model were unsuitable as they were not able to capture the highly non-linear response of the material. The MR and OG models were promising, but had some issues that will be discussed in Section 5. As a result, the BB model [14], which is commonly used to model rubber-like materials, was chosen as the basis for the numerical study in this article.

The short introduction to the BB model was provided in Section 1. Looking into it in more detail, it can be seen from the rheological model in Fig. 10a that the response is split in two parts. Part A accounts for the time-independent equilibrium response, and Part B represents the time-dependent response. Further, the deformation in Part B is multiplicatively split between a non-linear viscous dashpot and a hyperelastic spring. The response of Part A is given by the equation:

$$\bar{\tau}_A = \frac{\mu_A \lambda_{lock,A}}{3\lambda_c} \mathscr{L}^{-1}\left(\frac{\lambda_c}{\lambda_{lock,A}}\right)\bar{\boldsymbol{B}}_{iso} \tag{1}$$

where $\bar{\tau}_A$ is the deviatoric Kirchhoff stress tensor in Part A, μ_A is the shear modulus, $\lambda_{lock,A}$ is the locking stretch, λ_c is the effective chain stretch, $\mathscr{L}^{-1}(x)$ is the inverse Langevin function, and $\bar{\boldsymbol{B}}_{iso}$ is the deviatoric isochoric left Cauchy-Green deformation tensor. Similarly, the stress in Part B is given by the same hyperelastic relation, yet with a separate set of material constants:

$$\bar{\tau}_B = \frac{\mu_B \lambda_{lock,B}}{3\lambda_v} \mathscr{L}^{-1}\left(\frac{\lambda_v}{\lambda_{lock,B}}\right)\bar{\boldsymbol{B}}_{e,iso} \tag{2}$$

where $\bar{\tau}_B$ is the deviatoric Kirchhoff stress tensor in Part B, λ_v is the effective chain stretch based on the elastic part of the deformation and $\bar{\boldsymbol{B}}_{e,iso}$ is the elastic deviatoric left Cauchy-Green deformation tensor. The rate sensitivity of this model is captured through the evolution of the elastic left Cauchy-Green deformation tensor $\boldsymbol{B}_{e,iso}$:

$$\dot{\boldsymbol{B}}_{e,iso} = \bar{\boldsymbol{L}}\boldsymbol{B}_{e,iso} + \boldsymbol{B}_{e,iso}\bar{\boldsymbol{L}}^T - 2\boldsymbol{D}_i\boldsymbol{B}_{e,iso} \tag{3}$$

where $\dot{\boldsymbol{B}}_{e,iso}$ is the rate of $\boldsymbol{B}_{e,iso}$, $\bar{\boldsymbol{L}}$ is the deviatoric part of the velocity gradient and $\boldsymbol{D}_i$ is the inelastic rate of deformation. $\boldsymbol{D}_i$ is constitutively prescribed as:

$$\boldsymbol{D}_i = \dot{\gamma}\frac{\bar{\tau}_B}{||\bar{\tau}_B||} \tag{4}$$

with $\dot{\gamma}$ being the effective inelastic shear rate, defined as:

$$\dot{\gamma} = \dot{\gamma}_0(\lambda_i - 0.999)^c\left(\frac{||\bar{\tau}_B||}{\hat{\tau}\sqrt{2}}\right)^m \tag{5}$$

where $\dot{\gamma}_0$ is a reference inelastic shear rate, λ_i is the effective chain stretch of the inelastic part of the deformation, c and m are material constants and $\hat{\tau}$ is a reference effective shear stress. It should be noted that $\lambda_i \geq 1$.

The behaviour of the BB model subjected to large deformations will generally follow a given pattern. Initially the dashpot in Fig. 10a is locked, and both springs will be subjected to the same deformation. Depending on the effective shear stress in Part B and the rate of deformation, the dashpot will gradually unlock. This will limit the elastic deformations of the spring in Part B, such that $\bar{\tau}_B$ stabilizes, resulting in an additive rate sensitivity. It can be seen from Equation (5) that $\dot{\gamma}$ is dependent on the inelastic chain stretch as well, such that the viscous stress will not remain constant for a constant rate of deformation.

The experimental observations presented in Section 3.1 suggest that there is a significant multiplicative component to the rate sensitivity of the material, while the BB model exhibits primarily an additive rate sensitivity. Thus, a phenomenological extension to the BB model, as seen in Fig. 10b, is proposed to capture the multiplicative component of the rate sensitivity. The motivation for choosing this particular extension was to retain the simplicity and general behaviour of the BB model, while adding as few new parameters as possible. The proposed expansion is obtained by multiplying the stress in Part A with a Cowper-Symonds rate sensitivity factor:

$$\bar{\tau}_{A,BBmod} = \bar{\tau}_A\left(1 + sgn(\dot{\psi}_A)\left[\frac{\dot{\bar{\varepsilon}}}{\dot{\varepsilon}_0}\right]^R\right) \tag{6}$$

where $\bar{\tau}_A$ is the Kirchhoff stress defined in Equation (1), $\dot{\bar{\varepsilon}}$ is an effective

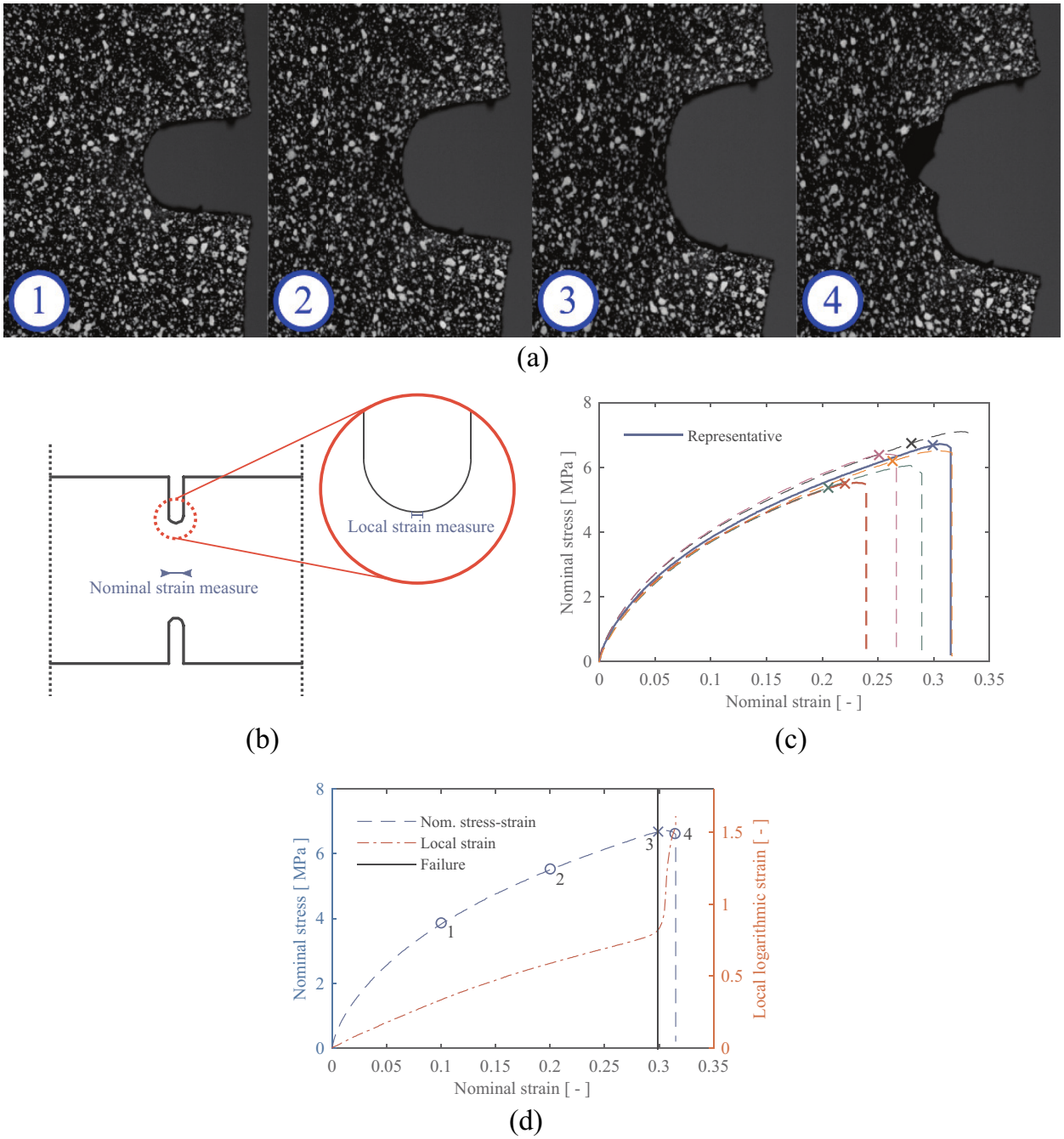

Fig. 8. Notched tension test results. a) Deformation states, with corresponding numbers in Fig. 8d, of representative test. (b) Definitions of different strain measures on notched specimens. (c) Overview of nominal stress strain for notched tensile specimens, with failure marked by '×' (d) Determination of failure strains for representative test. Numbers represent deformation states shown in Fig. 8a.

strain rate, $\dot{\varepsilon}_0$ is a reference strain rate, R is a material parameter and $\dot{\psi}_A$ is the time derivative of the eight-chain potential for the elastic component of the stress in Part A. The factor $sgn(\dot{\psi}_A)$ is introduced to ensure positive dissipation.

Both models were implemented in Abaqus Standard as a user-defined material model (UMAT). No fracture criterion was included, hence, the failure process at the end of the tests will not be captured by the numerical simulations.

4.2. Calibration and uniaxial results

Calibration of the two material models was done with MATLAB using a least square fit method and assuming incompressibility. The calibration process involved three steps:

1. The time independent parameters μ_A and $\lambda_{lock,A}$ were fitted to the tension test performed at a nominal rate of $10^{-3}s^{-1}$, while keeping the other parameters fixed at values that yielded zero contribution.
2. The time dependent parameters μ_B, $\lambda_{lock,B}$, $\dot{\gamma}_0$, $\hat{\tau}$, c, m, $\dot{\varepsilon}_0$ and R were fitted to six representative tests in both tension and compression at different rates, with the time independent parameters fixed.
3. Applying the parameters found in the two first steps as initial values, all parameters were relaxed and optimized to fit all six representative tests.

A comparatively high bulk modulus of 1000MPa was assumed to

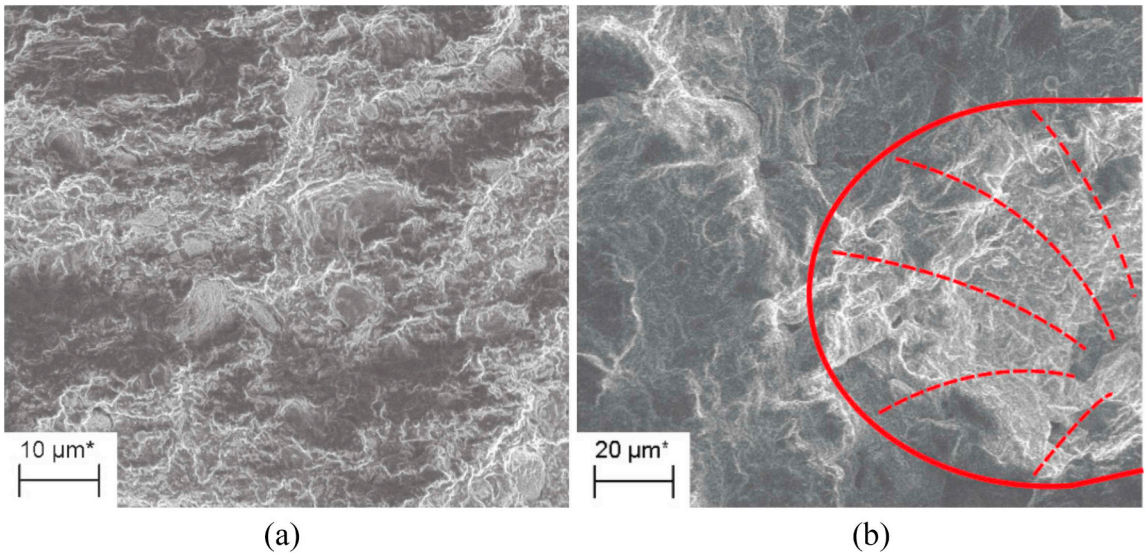

Fig. 9. SEM micrographs of the fractured surface of a notched specimen. (a) SEM image with magnification factor of 726 of a representative area of the fractured surface. (b) SEM image with magnification factor 357 of fracture surface likely in area of failure initiation.

ensure approximate incompressibility, thereby avoiding use of a hybrid formulation. The calibrated parameters for both models are presented in Table 2, and Fig. 11 shows comparisons between the test data and the fitted models.

Overall, the fit of both material models is seen to be satisfactory. However, it is evident that both models overestimate the initial stiffness in all cases except for the highest rate of deformation in compression. This is caused by the formulation of the effective inelastic shear rate described by the Equation (5), as it increases rapidly leading to an almost discontinuous response. The BBmod model yields slightly better results than the BB model due to a portion of the viscous response being represented by the smooth formulation given by Equation (6).

4.3. Validation

For validation of the two material models, the notched tensile test was analysed applying the model parameters given in Table 2. A full 3D finite element model with two symmetry planes was used to perform the analyses. The mesh consisted of linear hexahedral elements with varying sizes from 0.1mm inside the notch to 0.6mm at the edges as seen in Fig. 12. It should be noted that the mesh size inside the notch matched the initial length of the virtual extensometer for the local strain measure.

Preliminary numerical studies suggested that the notched tests exhibited primarily a uniaxial tension stress state. However, there were large stress gradients in the region around the sharp notch, featuring also an elevated stress triaxiality ratio and shear stresses. Such stress states are typically observed in various configurations of bonded joints, ensuring that this validation case is relevant. In addition, due to the non-uniformity of the deformation field, it is possible to extract multiple relevant measures for comparisons. In this case, the nominal and local measures defined in Section 3.4 were used for comparison.

Considering a representative experiment and the corresponding simulation, Fig. 12a shows the nominal stress and local strain plotted against the nominal strain. The overall impression is that the results agree satisfactory, and the numerical predictions approach the measured test data before failure. Recall that no failure model was included in the implementation used in this article, thus, simulation data past failure in the experimental test are irrelevant. Similar to what was observed for the stress-strain curves in Section 4.2, the overall performance of the BBmod model was slightly better than the BB model. The difference is more significant for the validation case, as a large part of the specimen was at a low strain level where the difference between the two models were more pronounced.

For both material models, the local response is seen to deviate from the test data almost immediately. Fig. 12b displays how the effective

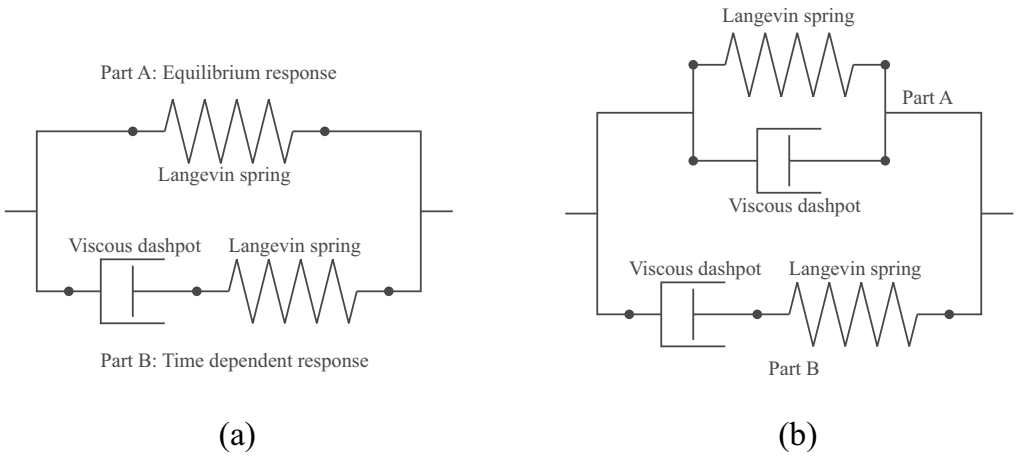

Fig. 10. Rheological models of the two implemented material models. (a) Bergström-Boyce rheological model. (b) Bergström-Boyce modified rheological model.

Table 2
Calibrated material parameters.

Model	BB parameters								BBmod param.	
	μ_A[MPa]	$\lambda_{lock,A}$[-]	μ_B[MPa]	$\lambda_{lock,B}$[-]	$\dot{\gamma}_0$[s^{-1}]	$\hat{\tau}$ [MPa]	c [-]	m [-]	$\dot{\varepsilon}_0$ [s^{-1}]	R [-]
BB	4.40	3.98	16.0	2.42	0.001	2.42	-1.56	6.68	-	-
BBmod	3.68	2.90	12.0	2.48	0.001	3.23	-3.21	13.7	68.0	0.267

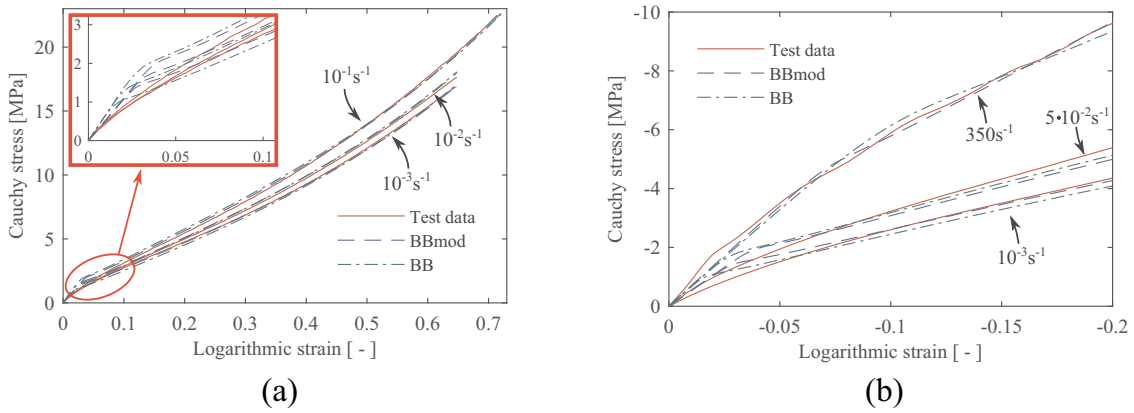

Fig. 11. Calibrated material models compared to test data in tension and compression at different strain rates. (a) Calibration results in tension for BB and BBmod. (b) Calibration results in compression for BB and BBmod.

inelastic shear rate is distributed in the numerical model before and after the simulation starts to deviate from the test data. It can be seen from State 1 that there is no inelastic shear rate on the front surface of the specimen where the local strain is measured. For State 2, there is significant inelastic shearing in that location. It can be seen from Equations 2, 3 and 4 that this inelastic shearing would reduce the contribution from Part B. This stiffness reduction leads to spurious strain localization, which is causing the deviation from the test data.

The nominal stress was generally underestimated in the simulations, which is believed to be linked to the same phenomenon on a global scale. It can be seen from Fig. 12 that for State A the inelastic shearing was localized in the notch. Therefore, the global response was dominated by the overly stiff initial material behaviour as seen in Section 4.2. For State B, the inelastic shear rate was activated throughout most of the specimen. However, the accumulated inelastic shear strain was localized in the notched section where the nominal strain was measured. This caused an overestimation of the nominal strain, which would contribute to the observed deviation from the test data. Towards the end of the deformation process, it was seen that the inelastic shear strain rate had a significant value in most of the specimen. This would alleviate the previous localization effect, such that the simulation converges towards the test data. In summary, it is seen that the smooth response observed in the test data is not properly captured due to the abrupt change in inelastic shear rate, for both the local and the global response. This is the same phenomenon as observed in Section 4.2, but amplified due to the non-uniformity of the deformation field.

5. Discussion

The experimental results indicate that the material studied in this article exhibit some of the phenomena reported in previous investigations on PU based adhesives in bulk form [6,12,13]. Specifically, large elastic deformations and rate sensitivity were observed. However, the stress levels in the previous studies are significantly different from what was measured in this work. Lubowiecka et al. [12] and Golaz et al. [13], applied a NH model and OG model to their respective adhesives with success. As mentioned in Section 4.1, these models were considered for the material studied in this article. While the NH model was deemed unsuitable, the OG model with linear viscoelasticity would likely give a perfect fit to the uniaxial test data as well as avoiding the issue with the inelastic shear rate. A problem with an OG model is that it is entirely phenomenological, which could lead to unphysical behaviour when it is subjected to deformation modes not used in the calibration process. Therefore, it would be strongly recommended to perform additional experiments that represent different deformation modes, e.g. pure shear and biaxial tension. These experiments are non-trivial to design and produce for the material studied in this article due to the low stiffness and large elastic deformations. In contrast to a phenomenological model, the BB model is based on micro-mechanical considerations, which according to Bergström [14] ensures that the behaviour when subjected to general load-cases is less prone to predict a non-physical response. Additionally, this class of models generally requires fewer parameters to obtain similar accuracy, making it easier to calibrate as well as reducing the associated costs. As shown in Section 4, the BB model with relatively few parameters yields satisfactory results when compared to the experimental data gathered in this work. The validation case in Section 4.3 does not guarantee that the models are well behaved for general load-cases, but it does serve as an indication, and it is likely that they would provide reasonably accurate predictions in tension and shear dominated load cases. Although the BBmod model serves as a phenomenological extension to the BB model, it is believed to retain a similar behaviour as the BB model when exposed to general load-cases. As shown by Equation (6), the modification is just a scaling of one of the components of the BB model.

Failure was omitted in the models implemented in Section 4, but the results presented in Section 3 could be used for determining a suitable model. All the tension tests were seen to fail in a brittle manner as expected from a material that does not exhibit plasticity. The crack propagation velocity is lower than what is typical for brittle materials, but that is likely due to the low modulus elasticity of the material. In addition, none of the compression tests were seen to fail. The notched test results described in Section 3.4, show that failure does not necessarily occur in the critical section of a flawless specimen. Therefore, it is likely that the initial cavities and inclusions in the specimens were large enough to determine failure. This notion is further reinforced by the fact that the locally measured failure strain in the notch is larger than in the tensile specimen.

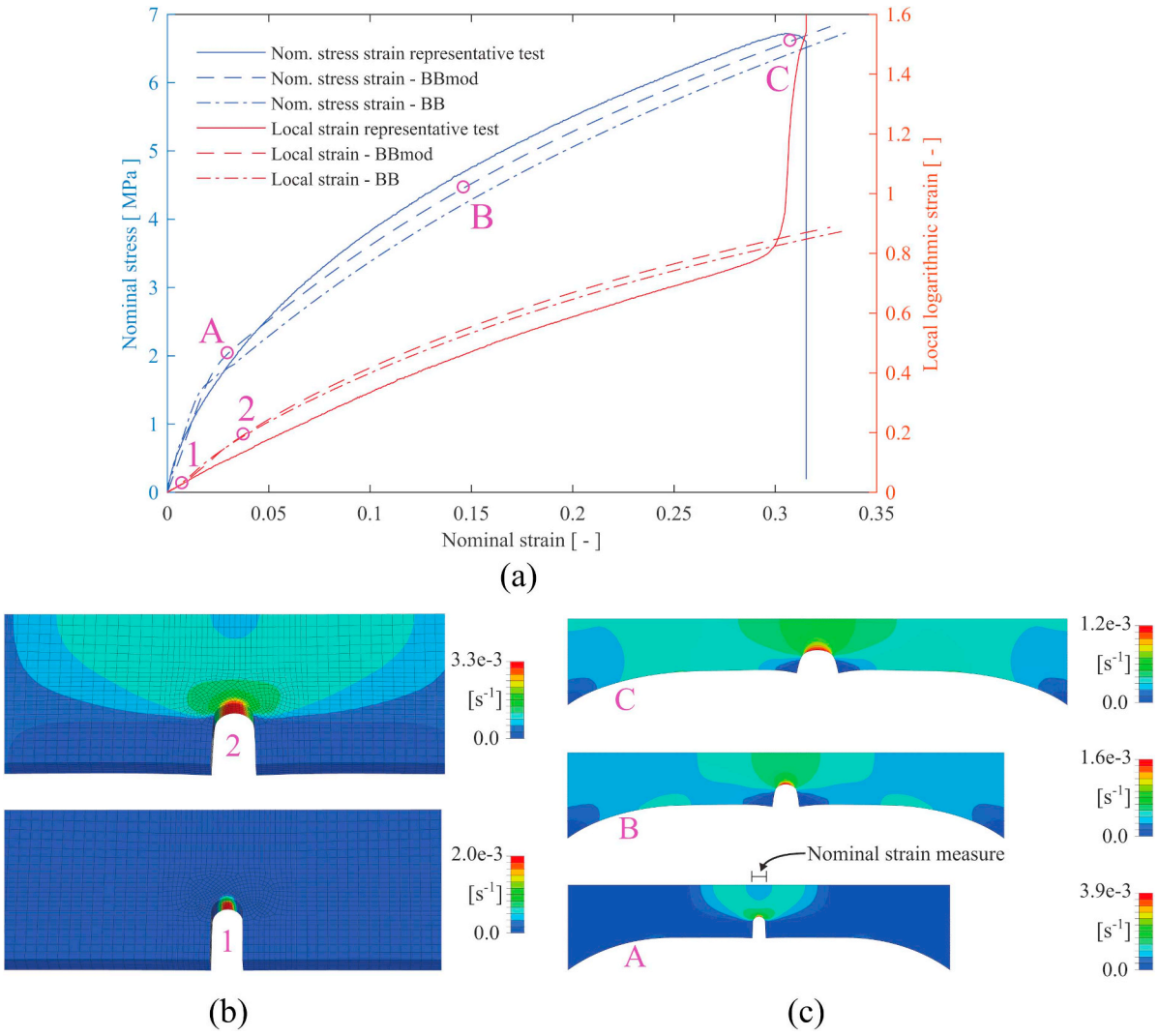

Fig. 12. Simulation results for the notched test specimen. Field outputs are taken from simulation using BBmod. (a) Comparison between simulations with two different material models and key responses from representative experimental test. (b) Field output of $\dot{\gamma}$ for states 1 and 2 in Fig. 12a. (c) Field output of $\dot{\gamma}$ for states A, B and C in Fig. 12a.

6. Conclusion

The key phenomena governing the behaviour of the semi-structural adhesive Betaforce 2816L were explored in the experimental part of this study. There were performed tests at several rates in both tension and compression to identify the rate sensitivity of the material. All experiments were monitored using DIC, which meant that deformation field data could be collected. Using several cameras, it was confirmed that the material was incompressible. In addition, brittle failure occurring inside the specimen was identified by the accelerated local strain on the surface of the specimen. Another important observation with respect to the choice of material model was that the plastic deformations as well as the adiabatic self-heating were insignificant.

It was evident from the experimental results that the typical plasticity-based framework for mesoscopic modelling of adhesives is not suitable for this class of semi-structural adhesives because plastic deformations are negligible. On the other hand, a micro-mechanically based model in the form of the Bergström-Boyce model was seen to give satisfactory results with the available test data. However, it was shown that there was a mismatch between experiments and the numerical models for small deformations when using the BB model. This was caused by the formulation of the inelastic shear rate, as it was too sensitive to capture the smooth response observed in the experiments. A modification to the BB model was implemented in an attempt to alleviate this issue by adding a multiplicative component to the rate sensitivity. Though the results were seen to be slightly better, a more comprehensive modification would be required to capture the initial response.

Acknowledgements

The financial support of this work from the Centre for Advanced Structural Analysis (CASA), Centre for Research-based Innovation (SFI) at the Norwegian University of Science and Technology (NTNU) through the Norwegian Research Council with the project number 237885, is gratefully acknowledged. Special thanks go to PhD Joakim Johnsen for the assistance with the numerical implementation, MSc Sindre Nordmark Olufsen for the CT scans, and MSc Christian Oen Paulsen for the SEM images.

References

[1] Martinsen K, Hu SJ, Carlson BE. Joining of dissimilar materials. CIRP Ann - Manuf Technol 2015;64:679–99. https://doi.org/10.1016/j.cirp.2015.05.006.
[2] da Silva LFM, Dillard DA, Blackman B, Adams RD. Testing adhesive joints: best practices. John Wiley & Sons; 2012. https://doi.org/10.1002/9783527647026.
[3] Hasegawa K, Crocombe AD, Coppuck F, Jewell D, Maher S. Characterising bonded

joints with a thick and flexible adhesive layer. part 2: modelling and prediction of structural joint responses. Int J Adhesion Adhes 2015;63:158–65. https://doi.org/10.1016/j.ijadhadh.2015.09.004.
[4] Dufour L, Bourel B, Lauro F, Haugou G, Leconte N. A viscoelastic-viscoplastic model with non associative plasticity for the modelling of bonded joints at high strain rates. Int J Adhesion Adhes 2016;70:304–14. https://doi.org/10.1016/j.ijadhadh.2016.07.015.
[5] Campilho RDSG, Banea MD, Neto JABP, da Silva LFM. Modelling adhesive joints with cohesive zone models: effect of the cohesive law shape of the adhesive layer. Int J Adhesion Adhes 2013;44:48–56. https://doi.org/10.1016/j.ijadhadh.2013.02.006.
[6] Jia Z, Yuan G, Ma H-l, Hui D, Lau K-t. Tensile properties of a polymer-based adhesive at low temperature with different strain rates. Compos B Eng 2016;87:227–32. https://doi.org/10.1016/j.compositesb.2015.10.013.
[7] Morin D, Haugou G, Bennani B, Lauro F. Experimental characterization of a toughened epoxy adhesive under a large range of strain rates. J Adhes Sci Technol 2011;25:1581–602. https://doi.org/10.1163/016942410X524417.
[8] Duncan B, Dean G. Measurements and models for design with modern adhesives. Int J Adhesion Adhes 2003;23:141–9. https://doi.org/10.1016/S0143-7496(03)00006-X.
[9] Morin D, Haugou G, Bennani B, Lauro F. Identification of a new failure criterion for toughened epoxy adhesive. Eng Fract Mech 2010;77:3481–500. https://doi.org/10.1016/j.engfracmech.2010.09.016.
[10] Morin D, Bourel B, Bennani B, Lauro F, Lesueur D. A new cohesive element for structural bonding modelling under dynamic loading. Int J Impact Eng 2013;53:94–105. https://doi.org/10.1016/j.ijimpeng.2012.02.003.
[11] Leuschner M, Fritzen F, van Dommelen JAW, Hoefnagels JPM. Potential-based constitutive models for cohesive interfaces: theory, implementation and examples. Compos B Eng 2015;68:38–50. https://doi.org/10.1016/j.compositesb.2014.08.024.
[12] Lubowiecka I, Rodríguez M, Rodríguez E, Martínez D. Experimentation, material modelling and simulation of bonded joints with a flexible adhesive. Int J Adhesion Adhes 2012;37:56–64. https://doi.org/10.1016/j.ijadhadh.2012.01.010.
[13] Golaz B, Michaud V, Månson JAE. Adhesion of thermoplastic polyurethane elastomer to galvanized steel. Int J Adhesion Adhes 2011;31:805–15. https://doi.org/10.1016/j.ijadhadh.2011.07.009.
[14] Bergström JS. Mechanics of solid polymers: theory and computational modeling. William Andrew; 2015. https://doi.org/10.1016/C2013-0-15493-1.
[15] Bergström JS, Boyce MC. Constitutive modeling of the large strain time-dependent behavior of elastomers. J Mech Phys Solids 1998;46:931–54. https://doi.org/10.1016/S0022-5096(97)00075-6.
[16] Arruda EM, Boyce MC. A three-dimensional constitutive model for the large stretch behavior of rubber elastic materials. J Mech Phys Solids 1993;41:389–412. https://doi.org/10.1016/0022-5096(93)90013-6.
[17] Johnsen J, Grytten F, Hopperstad OS, Clausen AH. Influence of strain rate and temperature on the mechanical behaviour of rubber-modified polypropylene and cross-linked polyethylene. Mech Mater 2017;114:40–56. https://doi.org/10.1016/j.mechmat.2017.07.003. Supplement C.